Journal of Computational Physics **172,** 658–684 (2001)
doi:10.1006/jcph.2001.6847, available online at http://www.idealibrary.com on IDEAL®

A Semi-Lagrangian High-Order Method for Navier–Stokes Equations

Dongbin Xiu and George Em Karniadakis[1]

Division of Applied Mathematics, Brown University, Providence, Rhode Island 02912
E-mail: gk@cfm.brown.edu

Received August 18, 2000; revised May 15, 2001

We present a semi-Lagrangian method for advection–diffusion and incompressible Navier–Stokes equations. The focus is on constructing stable schemes of second-order temporal accuracy, as this is a crucial element for the successful application of semi-Lagrangian methods to turbulence simulations. We implement the method in the context of unstructured spectral/*hp* element discretization, which allows for efficient search-interpolation procedures as well as for illumination of the nonmonotonic behavior of the temporal (advection) error of the form: $\mathcal{O}(\Delta t^k + \frac{\Delta x^{p+1}}{\Delta t})$. We present numerical results that validate this error estimate for the advection–diffusion equation, and we document that such estimate is also valid for the Navier–Stokes equations at moderate or high Reynolds number. Two- and three-dimensional laminar and transitional flow simulations suggest that semi-Lagrangian schemes are more efficient than their Eulerian counterparts for high-order discretizations on nonuniform grids.

1. INTRODUCTION

The case against direct numerical simulation of turbulent flows (DNS) at high Reynolds number (*Re*) is often made based on the enormous amount of spatial scales that need to be resolved. Indeed, simple estimates based on the Kolmogorov dissipative length scale suggest that the required number of degrees of freedom scale as $Re^{9/4}$ in three dimensions [17]. What is not factored, however, in such an estimate is the computational cost associated with the *time-integration* of the Navier–Stokes equations, which in practice, may be the prohibitive factor. After all, in a parallel computation, the spatial resolution requirements can be alleviated by domain decomposition whereas the time-stepping cost cannot be avoided.

To illustrate the current inefficiency of time-discretization, let us consider the often-used semi-implicit Eulerian scheme, where advection is treated explicitly. The maximum

[1] Corresponding author, gk@cfm.brown.edu.

0021-9991/01 $35.00

allowable time step is dictated by the *CFL* number, which is typically of order one, and thus

$$\Delta t_{CFL} \propto \frac{\mathcal{L}}{uN^{\alpha}}.$$

Here $\mathcal{L}$ is an integral length scale, u is a characteristic velocity scale, e.g., the *rms* value, and N^{α} represents the scaling of the maximum eigenvalue associated with the spectral discretization, with N the total number of nodes in one dimension. For example, for a Fourier discretization $\alpha = 1$; for Chebyshev discretization (used often in DNS of wall-bounded turbulence) $\alpha = 2$; and for spectral/hp element methods $\alpha \approx 3/2$ (see [18], Ch. 6). We want to compare this time step to the Kolmogorov time scale

$$\tau = \sqrt{(\nu\mathcal{L}/u^3)}.$$

To this end, we recall that according to Kolomogorov theory valid at high Reynolds numbers *Re*, in order to resolve the Kolmogorov *spatial* length scale, we need to employ approximately

$$N \approx Re^{3/4}$$

nodes per each spatial direction. Using these estimates, we can obtain the ratio of the maximum allowable time step to Kolmogorov's time scale, i.e.,

$$\frac{\Delta t_{CFL}}{\tau} \propto Re^{1/2}\frac{1}{N^{\alpha}} \propto Re^{1/2-3\alpha/4}. \tag{1}$$

It is clear from Eq. (1) that at Reynolds number of 10,000, the maximum allowable time step can be one order ($\alpha = 1$) to four orders ($\alpha = 2$) of magnitude smaller than the *temporal* Kolmogorov scale. Therefore, in most *spectral* DNS of *inhomogeneous* turbulence (where $\alpha \geq 3/2$), there is an *uneven distribution of resolution* in space and time, with the smallest spatial scale approximately matched but with the temporal scale over-resolved by at least two to three orders of magnitude.[2] This inefficiency of currently employed semi-implicit schemes for DNS of inhomogeneous turbulence has been recognized before, and attempts have been made to employ fully implicit schemes. However, this requires Newton iterations and nonsymmetric solvers that render the overall approach inefficient.

Progress can be made by employing semi-Lagrangian time-discretization, which could increase significantly the maximum allowable time step while maintaining the efficiency of symmetric solvers. The semi-Lagrangian approach has long been used in meteorology for numerical weather prediction, where the use of a large time step is essential for efficiency. This approach has been introduced at the beginning of the 1980s [31], and the basic idea is to discretize the Lagrangian derivative of the solution in time instead of the Eulerian derivative. It involves backward time integration of a characteristic equation to find the departure point of a fluid particle arriving at an Eulerian grid point. The solution value at the departure point is then obtained by interpolation. There is no mesh deformation as in Lagrangian methods because the "arrival points" employed coincide with the grid points.

[2] One could argue that discretization in space is typically high order but in time is low order; however, even with this factor taken into account the uneven distribution argument is still valid.

However, there may be significant interpolation cost to obtain the solution values at the "departure points."

The cost-effectiveness of semi-Lagrangian advection in the context of geophysical flows was studied systematically by Bartello and Thomas [4]. They found that there is significant computational overhead and that the efficiency of the semi-Lagrangian approach depends on the specific flow problem. For example, for quasi-geostrophic turbulence, the efficiency is high but for the Kolmogorov cascade the semi-Lagrangian scheme is efficient only at very high spatial resolutions. This result is consistent with the aforementioned analysis (e.g., case of uniform discretization $\alpha = 1$) if we take into account the computational overhead associated with semi-Lagrangian advection. The analysis in [4] involves homogeneous turbulence only, and comparisons with a relatively low-order Eulerian scheme with at most cubic spline interpolations. The method we develop here targets complex-geometry flows with truly high-order spatial discretizations that require nonuniform grids. Our experience with such flows using Eulerian time stepping is that they require time steps much smaller than what accuracy considerations dictate; e.g., see [6, 22].

The semi-Lagrangian method depends strongly on the spatial discretization. Specifically, its accuracy is particularly sensitive to the method of backward integration of the characteristic equation as well as the interpolation scheme to evaluate the solution at departure points. This has been shown by Falcone and Ferretti [9], who conducted a rigorous analysis of the stability and convergence properties of semi-Lagrangian schemes. Typically, the backward integration is performed by employing second-order schemes (i.e., midpoint rule), explicitly or implicitly. In [15] and [21], the fourth-order Runge–Kutta method was employed but their results did not show any improvement over the second-order schemes. This finding is perhaps due to low spatial resolution used in these works, which is crucial for the overall accuracy of semi-Lagrangian schemes. It has been shown that the simplest semi-Lagrangian scheme with linear interpolation is equivalent to the classical first-order upwinding scheme [27], which is excessively dissipative (see [31] and [37]). A popular and effective choice for interpolation methods in previous works has been the cubic spline methods [20]; see also [4].

An intriguing finding is that the error of semi-Lagrangian schemes in solving advection–diffusion equations *decreases* as the time step increases in a certain range of parameters, and this has initially led to some erroneous justifications [24, 25]. The error analysis in [9] showed that the overall error of semi-Lagrangian method is indeed *not* monotonic with respect to time step Δt, and, in particular, it has the form

$$\mathcal{O}\left(\Delta t^k + \frac{\Delta x^{P+1}}{\Delta t}\right),$$

where k refers to the order of backward time integration and P to the interpolation order; similar conclusions had been reached earlier in [23]. Another interesting result was obtained by Giraldo [13] who combined the semi-Lagrangian approach with spectral element discretization for the advection–diffusion equation. He found that for polynomial order $P \geq 4$ the combined scheme exhibits neither dissipation nor dispersion errors. This important result has to also be factored into any cost-effectiveness analysis regarding semi-Lagrangian advection.

The extension of semi-Lagrangian method to the solution of Navier–Stokes equations was presented in the pioneering work of Pironneau (1982) [28]. He demonstrated the nonlinear

stability of the method even as the viscosity approaches to zero. He also obtained suboptimal error estimates, which were improved later by Süli (1988) [38]. Most of the previous analysis and numerical implementations in CFD applications have employed the Taylor–Hood finite element and are first-order in time [2, 15, 29]. In a more recent paper [1], an error analysis was conducted for the fractional-step method for incompressible Navier–Stokes equations. In particular, the pressure–correction version of the fractional scheme with first-order time stepping was analyzed and an extension to a second-order was proposed but not analyzed. An attempt at a second-order scheme was made in [2] but no convergence rates were documented in that work. Moreover, results presented for the standard benchmark problem of driven-cavity flow are markedly different than accepted results in the literature, possibly because of an erroneous treatment of the pressure term. A higher-order temporal discretization, similar to the stiffly-stable scheme proposed in the present paper, was proposed independently in [5] for advetion problems.

In this paper, we present a semi-Lagrangian spectral/*hp* element (SLSE) method for the two- and three-dimensional incompressible Navier–Stokes equations, inspired by the results of Giraldo [13] for the advection–diffusion equation. In particular, we apply the newer *modal* version of the spectral element method [18] to the advection diffusion; unstructured discretizations are involved consisting of triangles and tetrahedra. We study in detail the dependence of the overall accuracy upon the time step, demonstrating the non-monotonic trends suggested by the theory of Falcone and Ferretti [9]. We then extend the semi-Lagrangian spectral/*hp* element method to incompressible Navier–Stokes equations targeting a high-order temporal discretization. To this end, we propose a discretization based on a second-order stiffly-stable scheme, to circumvent instabilities or inaccuracies associated with the treatment of the pressure term in previous efforts. We demonstrate that the new SLSE method achieves second-order accuracy in time and retains spectral accuracy in space. We also demonstrate the nonmonotonic dependence of error upon time step for a certain range of parameters, similar to that of advection–diffusion equation. The new SLSE method is applied to two- and three-dimensional incompressible flow problems with typical time steps more than *twenty times* the time steps of the corresponding Eulerian discretization. Here we consider standard benchmarks for CFD for which there is plenty of experience using Eulerian time-stepping with various spatial discretization approaches. Both laminar and transitional flows are considered but not turbulent flows as they merit a separate investigation. As regards efficiency, a new search-interpolation procedure is developed, which makes the SLSE method at most twice as expensive *per time step* compared to its Eulerian counterpart for the *advection–diffusion* equation. For high spectral order ($P \geq 10$), the SLSE method is less than 25% more expensive per time step than the Eulerian approach, resulting in an overall gain *one-* to *two-orders of magnitude* in favor of the SLSE. For the Navier–Stokes simulations we performed, the overall speed-up depends on the specific case. The cost for the SLSE varies from four to ten times smaller than the computational cost of the corresponding Eulerian SE scheme with no special code optimization involved.

The paper is organized as follows: In the next section, we present the algorithms for search, interpolation, and backward integration, and validate the method for the advection–diffusion equation. We then extend the method to incompressible Navier–Stokes equations examining different splitting schemes, and present two- and three-dimensional flow simulations in the laminar and transition regime for validation of the method. We conclude with a brief summary.

2. ADVECTION–DIFFUSION EQUATION

We first consider the advection–diffusion equation

$$\frac{\partial \phi}{\partial t} + \mathbf{u} \cdot \nabla \phi = \nu \nabla^2 \phi, \tag{2}$$

and we use a semi-implicit scheme for time discretization, i.e., we employ a second-order Adams–Bashforth scheme for the advection term and a Crank–Nicolson scheme for the diffusion term

$$\frac{\phi^{n+1} - \phi^n}{\Delta t} + \mathbf{u} \cdot \nabla \left(\frac{3\phi^n - \phi^{n-1}}{2} \right) = \nu \nabla^2 \left(\frac{\phi^{n+1} + \phi^n}{2} \right). \tag{3}$$

The semi-implicit scheme avoids the stability constraint from the diffusion term but it is subject to the CFL condition because of the explicit treatment of the advection term. The CFL restriction is more severe for the spectral/hp element method as the permissible time step Δt scales approximately as the square of the spectral order [18].

The Lagrangian form of (2) is

$$\frac{d\phi}{dt} = \nu \nabla^2 \phi, \tag{4}$$

$$\frac{d\mathbf{x}}{dt} = \mathbf{u}(\mathbf{x}, t). \tag{5}$$

The idea of a *pure* Lagrangian approach is to solve Eq. (4) along the characteristic lines (5). This leads to an effective decoupling of the advection and diffusion terms and an unconditionally stable scheme. However, as the fluid particles move along, they may result in heavily distorted and irregular mesh. Hence, expensive remeshing is required between time steps. In the semi-Lagrangian approach, the computational mesh is *fixed*. At each time step, a discrete set of particles arriving at the grid points is tracked backward over a single time step along its characteristic line up to its departure points. The solution value at the departure points is then obtained by interpolation. The second-order Crank–Nicolson semi-Lagrangian scheme is of the form

$$\frac{\phi^{n+1} - \phi_d^n}{\Delta t} = \nu \nabla^2 \left(\frac{\phi^{n+1} + \phi_d^n}{2} \right), \tag{6}$$

$$\frac{d\mathbf{x}}{dt} = \mathbf{u}(\mathbf{x}, t), \quad \mathbf{x}^{n+1} = \mathbf{x}(t^{n+1}) = \mathbf{x}_a. \tag{7}$$

Here ϕ_d^n denotes the value of ϕ at the *departure* points $\mathbf{x}_d$ at time level n, and $\mathbf{x}_a$ is the position of the *arrival* points which are the grid points. The characteristic equation (7) is solved backward, i.e., we solve for the departure point at time level n, $\mathbf{x}_d^n$, with the initial condition $\mathbf{x}^{n+1} = \mathbf{x}_a$.

2.1. Details of the Algorithm

The departure points do not coincide with the grid points, and thus a search-interpolation procedure is needed. Also, the overall accuracy and efficiency of semi-Lagrangian depends critically on both the accuracy of the backward intergration of (7) as well as the accuracy of

the interpolation method. In the following, we provide details on how we implement both algorithms.

2.1.1. *Backward Integration*

We solve Eq. (7) for one single time step in order to obtain $\mathbf{x}_d = \mathbf{x}(t^n)$ by the explicit second-order midpoint rule

$$\hat{\mathbf{x}} = \mathbf{x}_a - \frac{\Delta t}{2}\mathbf{u}(\mathbf{x}_a, t^n), \tag{8}$$

$$\mathbf{x}_d = \mathbf{x}_a - \Delta t\ \mathbf{u}\left(\hat{\mathbf{x}}, t^n + \frac{\Delta t}{2}\right). \tag{9}$$

By defining

$$\alpha = \mathbf{x}_a - \mathbf{x}_d,$$

we can rewrite the *explicit* midpoint rule as

$$\alpha = \Delta t\ \mathbf{u}\left(\mathbf{x}_a - \frac{\Delta t}{2}\mathbf{u}(\mathbf{x}_a, t^n), t^n + \frac{\Delta t}{2}\right). \tag{10}$$

Similarly, we employ *implicit* integration for Eq. (8) setting

$$\hat{\mathbf{x}} = \mathbf{x}_a - \frac{\Delta t}{2}\mathbf{u}\left(\hat{\mathbf{x}}, t^n + \frac{\Delta t}{2}\right),$$

to arrive at the implicit midpoint rule

$$\alpha = \Delta t\ \mathbf{u}\left(\mathbf{x}_a - \frac{\alpha}{2}, t^n + \frac{\Delta t}{2}\right). \tag{11}$$

This is the backward integration algorithm used in most of previous semi-Lagrangian schemes. Although the explicit and implicit schemes are formally of second-order, a small accuracy improvement has been reported for the implicit method. Equation (11) has to be solved iteratively, but numerical experiments show that only a few iterations are needed for convergence (typically around five). This result is valid if a high-order predictor is employed in the iterative process [30, 34]. For an advection–diffusion equation with the velocity field known analytically, this additional cost is negligible. However, for a velocity field known only in numerical form, the iteration is costly because each substep requires a search-interpolation procedure. Our numerical results show that the two methods give almost identical results and for more general problems, especially for Navier–Stokes equations, the explicit method (Eq. (10)) is preferred. To enhance the accuracy further, higher-order methods can be used; in the following we will be using the fourth-order Runge–Kutta method.

2.1.2. *Search-Interpolation Procedure*

In general, the departure points do not coincide with the grid points. To evaluate the solution at these points, we have developed the following algorithms:

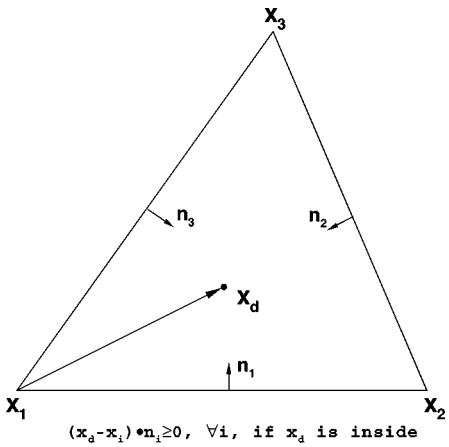

FIG. 1. Sketch to illustrate the searching algorithm.

Searching Algorithm. We first determine in which element a particular departure point lies. Although for structured grids this task can be as simple as index checking, it is nontrival for unstructured grids. For general quadrilaterals, the QuadTree algorithm has been employed by Giraldo [13]. In this paper, we present a new fast searching algorithm especially designed for the semi-Lagrangian method that works for triangles, quadrilaterals, tetrahedra, and hexahedra elements in unstructured discretizations.

The searching starts with the "parent" element, which could be the element where the point physically lies initially or where it is last found (see Fig. 1). To decide if the point is in the element or not, the scalar product between the vector starting from the vertex of the element to the point and the inward normal vertor of the corresponding edge is taken. The point is inside the element if all the scalar products of each edge are positive. If any of them is negative, the point falls outside the element in that direction. The searching is then moved to the neighboring element in that direction by using the connectivity information of the unstructured grid until the parent element is found. In the worst case scenario, the number of elements checked is the same as the number of elements the particle travels. Thus, the method is very fast; as in the spectral/*hp* element method, a substantially smaller number of elements is employed compared to low-order finite elements. Our numerical tests show that the cost of searching is negligible compared to the other costs.

Interpolation Algorithm. An advantage of the spectral/*hp* element method is that it employs a high-order polynomial basis and thus there is no need for constructing explicitly special interpolation functions (e.g., cubic splines). A Lagrangian interpolation is then performed in the parent element of the departure points using the spectral basis, which is a hierarchical set of Jacobi polynomials [18]. The order of the polynomial basis used throughout this paper ranges from $P = 1$ to $P = 14$ with a typical value $P = 8$.

2.2. Numerical Results

In this section we present the results and error analysis of the SLSE method applied to advection–diffusion equation (2).

2.2.1. *Benchmark Problem*

We use the same Guassian-cone problem, also used in [13], to test the SLSE method. The transport velocity field is

$$u = +y, \quad v = -x.$$

The initial condition is

$$\phi(x, y, 0) = e^{-[(x-x_0)^2+(y-y_0)^2]/2\lambda^2},$$

and the exact solution is

$$\phi(x, y, t) = \frac{\lambda^2}{\lambda^2 + 2\nu t} e^{-[\hat{x}^2+\hat{y}^2]/2(\lambda^2+2\nu t)},$$

where

$$\hat{x} = x - x_0 \cos t - y_0 \sin t, \quad \hat{y} = y + x_0 \sin t - y_0 \cos t.$$

The constants are fixed at $\lambda = \frac{1}{8}$; and $(x_0, y_0) = (-\frac{1}{2}, 0)$. A mesh consisting of 10×10 quadrilateral elements is used, and the time-integration is performed for *one revolution* corresponding to $t = 2\pi$.

The L^2 error norm is used to examine the accuracy, i.e.,

$$e_{L^2} = \frac{\int (\phi_{exact} - \phi)^2 \, d\Omega}{\int \phi_{exact}^2 \, d\Omega}. \tag{12}$$

The Courant number (CFL) and the nondimensional diffusion coefficient are defined as

$$\sigma = \max\left(\frac{U \Delta t}{\Delta s}\right) \quad \text{and} \quad \mu = \max\left(\frac{\nu \Delta t}{\Delta s^2}\right),$$

where $U = \sqrt{u^2 + v^2}$ and $\Delta s = \sqrt{\Delta x^2 + \Delta y^2}$; these definitions are the same as in [13].

In Fig. 2, we plot the results from an Eulerian method (Adams–Bashforth/Crank–Nicolson, ABCN) and the SLSE method with fixed $\sigma = 0.5$ and $\mu = 0.01$. The backward integration is the explicit midpoint rule (Eq. (10)), denoted here as RK2 method. The spectral order varies from $P = 2$ to 8. We observe on this semi-log plot that spectral convergence is achieved for both methods. The SLSE method gives relatively larger error at lower polynomial order P, but it quickly reaches the $\mathcal{O}(\Delta t^2)$ temporal error limit at $P = 8$. In Fig. 3, we plot the results with larger time step. The base time step Δt corresponds to CFL number $\sigma = 0.5$. Results with $10\Delta t$ and $20\Delta t$, which correspond to CFL number 5 and 10, are also plotted. We observe that as the time step increases, the error is reduced, matching the error of the Eulerian scheme but at time step size *twenty* times larger. Also, a further improvement with the fourth-order Runge–Kutta method (RK4) is obtained at $20\Delta t$ with polynomial order $P = 6$.

2.2.2. *Error Analysis*

The error of semi-Lagrangian method consists of two parts: the error of the backward integration $\mathcal{O}(\Delta t^{k+1})$ and the error from interpolation $E(\Delta x) = \mathcal{O}(\Delta x^{P+1})$, where k is

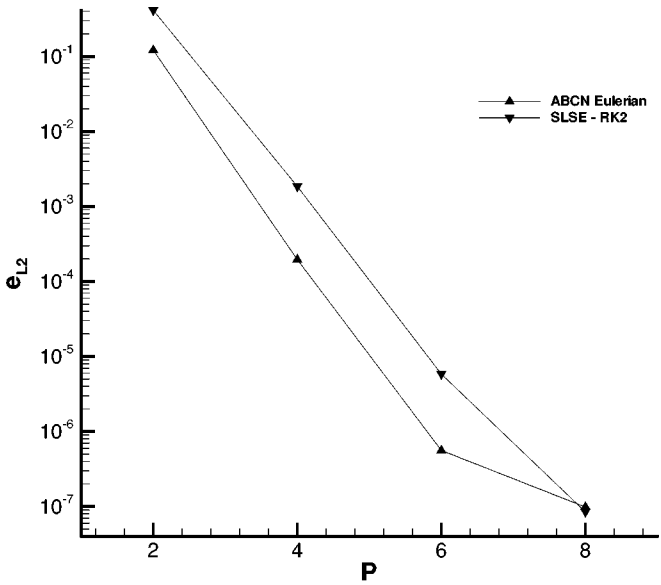

FIG. 2. Spatial convergence of Eulerian and semi-Lagrangian methods with a spectral/*hp* element discretization at small time step; Gaussian-cone problem.

the order of integration method and P is the order of the polynomial basis. Therefore, the overall accuracy of semi-Lagrangian method is

$$\frac{u^{n+1} - u_d^n}{\Delta t} = \frac{du}{dt} + \mathcal{O}\left(\Delta t^k + \frac{\mathcal{O}(\Delta x^{P+1})}{\Delta t}\right). \tag{13}$$

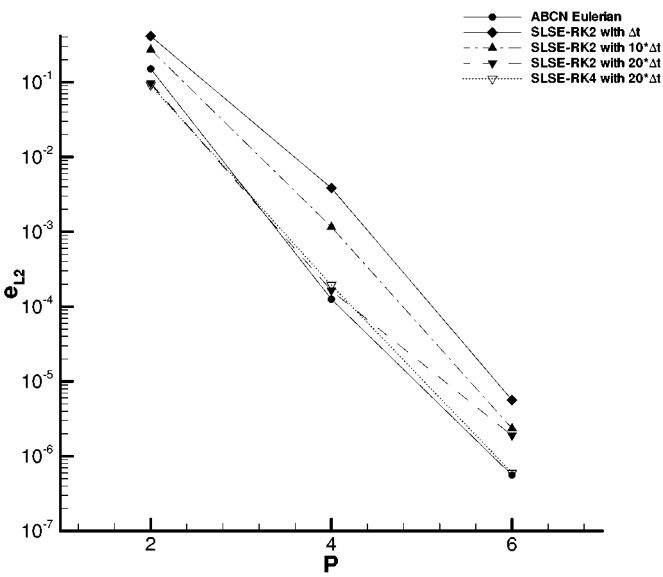

FIG. 3. Spatial convergence of Eulerian and semi-Lagrangian methods at large Δt; Gaussian-cone problem.

A rigorous derivation of the above expression can be found in [9]. Equation (13) shows that the error is not monotonic with respect to Δt. When the polynomial order P is small, the interpolation error dominates. As Δt increases, the overall error decreases. It can also be appreciated that as the first term $\mathcal{O}(\Delta t^k)$ is subdominant, further increasing k will not improve the overall accuracy. This explains the reason that [15] and [21] did not see improvement of fourth-order Runge–Kutta method over the second-order methods. On the other hand, when the spatial error is subdominant at high P, increasing Δt increases the first error term in [13] and thus the overall error is larger. In this case, a higher-order backward integration method (higher k, e.g., Runge–Kutta of fourth-order) reduces the dominant first term and improves the solution.

To further study the structure of the error, we test the SLSE method at different time steps and different spectral orders. We set the viscosity to a small value, $\nu = 4.6 \times 10^{-6}$, in order to emphasize the effect of the advection. The range for Δt is 0.01 to 0.05, which corresponds to CFL number 5 to 25, for $P = 10$. In Fig. 4 we plot results obtained with second-order backward integration ($k = 2$) in log–log axes. We make the following observations:

- $P = 4$: The interpolation error is relatively large, and thus the second error term in (13) dominates. As Δt increases, the overall accuracy improves almost monotonically up to a large Δt when the first error term becomes significant.
- $P = 6$: The interpolation error is smaller and the first error term in (13), $\mathcal{O}(\Delta t^2)$, is comparable with the second term. As Δt increases, the error starts to decrease first. The $\mathcal{O}(\Delta t^2)$ term then becomes dominant and the overall error starts to increase. At this intermediate spatial resolution, there is clearly a competition between the two error terms resulting in the minimum error around $\Delta t \approx 0.024$.
- $P = 8$: The interpolation error is sufficiently small and thus the $\mathcal{O}(\Delta t^2)$ dominates. The overall error then grows at an algebraic second-order rate.
- $P = 10$: The result is identical to that of $P = 8$, because the dominant error is the $\mathcal{O}(\Delta t^2)$ term, which does not depend on P.

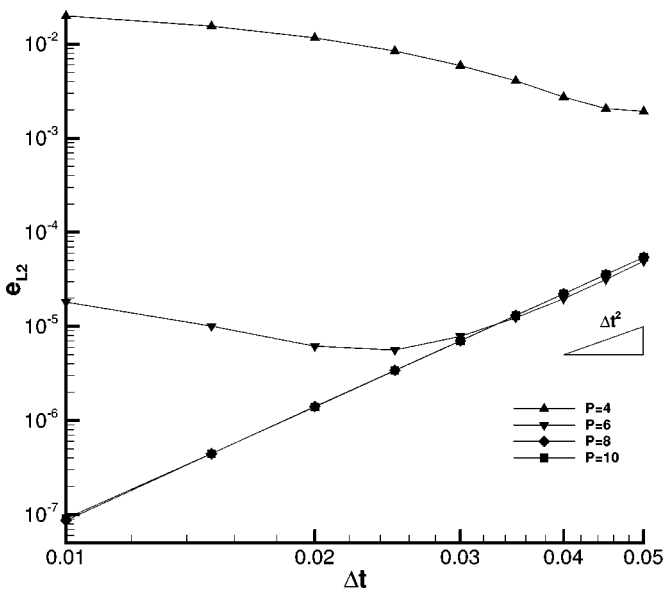

FIG. 4. Error dependence upon Δt with second-order backward integration for several spectral orders P.

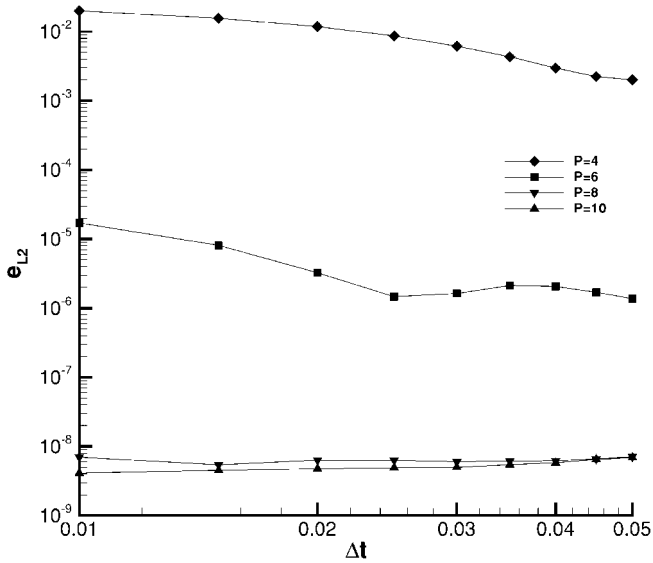

FIG. 5. Error dependence upon Δt with fourth-order Runge–Kutta for backward integration.

A similar but less obvious behavior can be observed in Fig. 5 with fourth-order Runge–Kutta backward integration ($k = 4$). It is worth noticing that with high-order interpolation polynomials, $P = 8$ and $P = 10$, the interpolation error is very small and so is the backward integration error ($\mathcal{O}(\Delta t^4)$). The competition between the two error terms results in a *plateau*, and the overall accuracy is preserved over a large range of time step. A slight anomaly is observed for $P = 6$ where a second decaying trend appears toward the larger step.

The above results show that when the solution is well-resolved in space with high-order polynomial interpolation, the overall accuracy is solely controlled by the method of backward integration. In Fig. 6, we plots results obtained with polynomial order $P = 10$; second-, third- and fourth-order Runge–Kutta backward integrations are employed and referred to in the legend as RK2, RK3, and RK4, respectively. The second-order scheme, RK2, shows an algebraic growth rate of order two, as the $\mathcal{O}(\Delta t^2)$ error term always dominates. For third- and fourth-order schemes, RK3 and RK4, the trend is less obvious. When Δt is not too large,

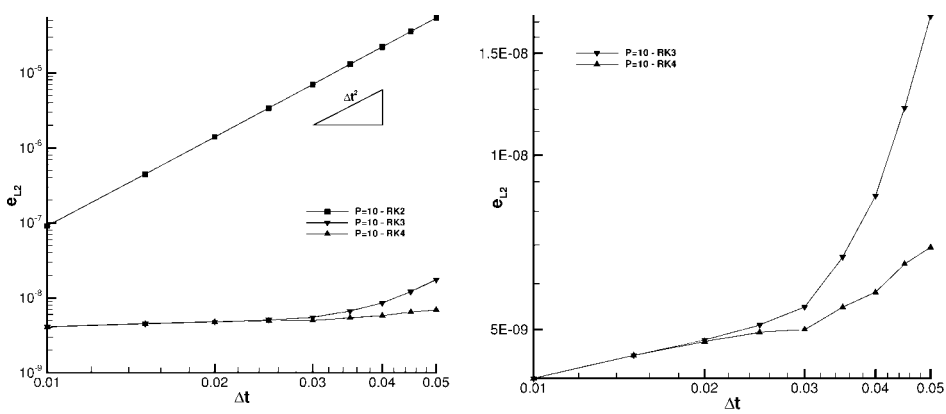

FIG. 6. Error dependence upon Δt with $P = 10$: Left: RK2, RK3, and RK4; Right: close-up view of RK3 and RK4.

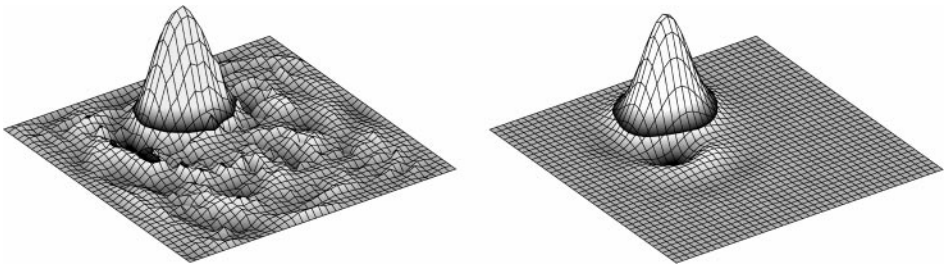

FIG. 7. Numerical solution for the parabolic cone advection problem. Left: Eulerian SE method, and Right: SLSE method. A low resolution $P = 4$ simulation is shown and the contour levels are nonuniform for visualization purposes. In both plots, the same exactly vizualization approach was employed.

the two error terms in the estimate (13) are comparable and the competition between them is nearly in balance resulting in a very slow growth in overall error. It is only at relatively large Δt that the two methods deviate and show different growth rates (see right plot).

2.2.3. *Solution of Finite Smoothness*

To further examine the accuracy and robustness of the SLSE method, we solved the advection equation for a solution with finite regularity. The initial condition is a parabolic cone, which has a discontinuity in the derivatives, unlike the previously tested smooth Gaussian cone,

$$\phi(x, y, t = 0) = \begin{cases} -16\left[r_0^2 - \frac{1}{16}\right] & \text{if } r_0 < \frac{1}{4} \\ 0 & \text{elsewhere'} \end{cases}$$

where $r_0^2 = (x - x_0)^2 + (y - y_0)^2$ and (x_0, y_0) is the initial center position of the cone. The transport velocity field is the same as used in the previous example. This problem is solved with both Eulerian and semi-Lagrangian spectral/*hp* element methods. A mesh consisting of 10×10 quadrilateral elements was used. For polynomial order $P = 4$, the two numerical solutions are compared in physical space in Fig. 7 after 10 revolutions. The point-wise error of the solution after one revolution is plotted in Fig. 8 for

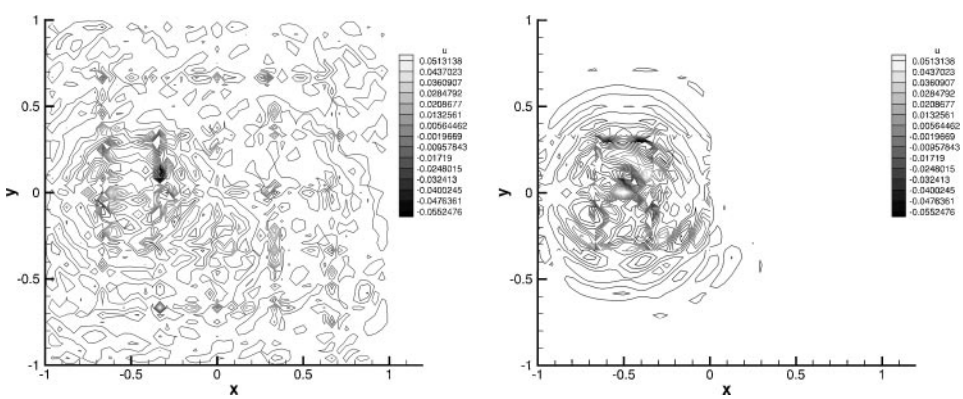

FIG. 8. Point-wise error for the parabolic cone advection problem. Left: Eulerian SE method. Right: SLSE method.

TABLE I
Comparison of Computational Cost of Eulerian SE and SLSE Methods

Polynomial order P	SLSE-RK4 (sec/step)	ABCN Eulerian (sec/step)	Ratio (SLSE/ABCN)	Overall speed-up (SLSE/ABCN)
4	0.15	0.08	1.88	10.6
6	0.39	0.21	1.86	10.8
8	0.80	0.51	1.57	12.7
10	1.49	1.19	1.25	16.0

polynomial order $P = 8$. We see that for both resolutions the errors for the SLSE method are localized near the discontinuity, in agreement with previously reported results [9]. However, for the Eulerian scheme error oscillations are spread everywhere in the domain.

2.2.4. *Computational Cost*

The SLSE method is generally more expensive *per time step* than its Eulerian counterpart. However, by using the fast searching algorithm presented above, the computational cost of SLSE can be of the same order as the Eulerian spectral/hp element method. In Table I we compare the computational cost of the two approaches for the aforementioned Gaussian-cone problem. We see that the SLSE method is less than twice more expensive than the Eulerian method, and as the spectral order increases the two costs are comparable. However, with much larger allowable CFL numbers, the total CPU time required for the SLSE method to reach a certain time level is significantly less than that of Eulerian method. The overall speed-up list in the table is obtained at CFL number of 20. Therefore, at least one order of magnitude in speed-up is achieved. The observed drop in the cost ratio as P increases can be explained as follows: In the current implementation of the SLSE method, the common edges of interior elements are calculated twice. As the number of degrees-of-freedom of these common edges counts for a smaller portion as P increases, the cost ratio decreases. No full optimization has been performed yet to further reduce the search-interpolation CPU time.

3. INCOMPRESSIBLE NAVIER–STOKES EQUATIONS

In this section, we extend the SLSE method to incompressible Navier–Stokes equations. Our goal is to design a robust scheme with high-order accuracy in time. We consider the Navier–Stokes equations in Lagrangian form

$$\frac{d\mathbf{u}}{dt} = -\nabla p + \nu \nabla^2 \mathbf{u}, \tag{14}$$

$$\nabla \cdot \mathbf{u} = 0, \tag{15}$$

and present three different time-discretization schemes.

3.1. The First-Order Scheme

The first-order semi-Lagrangian scheme can be obtained readily by treating the right-hand side of (14) implicitly, i.e.,

$$\frac{\mathbf{u}^{n+1} - \mathbf{u}_d^n}{\Delta t} = -\nabla p^{n+1} + \nu \nabla^2 \mathbf{u}^{n+1}, \tag{16}$$

$$\nabla \cdot \mathbf{u}^{n+1} = 0. \tag{17}$$

This approach leads to unconditional stability and has been used in [15, 28, 38]. However, it is only first-order in time and thus accuracy considerations limit its effectiveness.

3.2. The Second-Order Schemes

We propose two different approaches, the Crank–Nicolson scheme and the stiffly-stable scheme. We will show that only the latter is suitable for practical applications.

3.2.1. *Crank–Nicolson Scheme*

A direct extension of the Crank–Nicolson semi-Lagrangian method from the previous section yields

$$\frac{\mathbf{u}^{n+1} - \mathbf{u}_d^n}{\Delta t} = -\nabla p^{n+1} + \nu \nabla^2 \left(\frac{\mathbf{u}^{n+1} + \mathbf{u}_d^n}{2} \right), \tag{18}$$

$$\nabla \cdot \mathbf{u}^{n+1} = 0, \tag{19}$$

where $\mathbf{u}_d^n$ denotes the velocity $\mathbf{u}$ at the departure point $\mathbf{x}_d$ and time level t^n. The characteristic equation is

$$\frac{d\mathbf{x}}{dt} = \mathbf{u}^{n+\frac{1}{2}}(\mathbf{x}, t), \quad \mathbf{x}(t^{n+1}) = \mathbf{x}_a, \tag{20}$$

where $\mathbf{x}_a$ is the position vector of the arrival points, which coincide with the grid points. The velocity at $t^{n+1/2}$ is approximated by the second-order extrapolation

$$\mathbf{u}^{n+\frac{1}{2}} = \frac{3}{2}\mathbf{u}^n - \frac{1}{2}\mathbf{u}^{n-1}. \tag{21}$$

Equations (18) and (19) can be solved by the fractional-step method, where the discrete continuity equation results in a consistent Poisson equation for the pressure. This method seems to be second-order in time, and it has been used recently in [2]. However, our numerical experiments show that it is in fact still first-order in time. It can also be justified as follows: Considering the fact that the idea of semi-Lagrangian scheme is to integrate the Navier–Stokes equations (14) along characteristic lines, i.e.,

$$\int_{\mathbf{x}_d}^{\mathbf{x}_a} \frac{d\mathbf{u}}{dt}\, dt = \int_{\mathbf{x}_d}^{\mathbf{x}_a} (-\nabla p + \nu \nabla^2 \mathbf{u})\, d\mathbf{x}, \tag{22}$$

a *true* second-order approximation, according to the midpoint rule, should take the form

$$\frac{\mathbf{u}^{n+1} - \mathbf{u}_d^n}{\Delta t} = \frac{1}{2}\left[(-\nabla p + \nu \nabla^2 \mathbf{u})_d^n + (-\nabla p + \nu \nabla^2 \mathbf{u})^{n+1} \right]. \tag{23}$$

Second-order accuracy can be verified by performing a Taylor expansion analysis. Comparing the above equation with Eq. (18), it is clear that method (18) can be at most first order in time.

The method described in Eq. (23) can be implemented using a high-order splitting scheme, which results in a three-step procedure [16]. However, our numerical experiments show that this method develops a long-term instability in the computation. This is due to the explicit part of pressure term in (23), and it is similar to the long-term instability observed in the Eulerian pressure correction formulation [14, 18]; it could be treated by additional projections.

3.2.2. *Stiffly-Stable Scheme*

To circumvent the long-term instability resulted from the explicit part of pressure term (see results below), we employ a variation of the backward multistep scheme [11] to discretize the time derivative. A second-order time-discretization is

$$\frac{\frac{3}{2}\mathbf{u}^{n+1} - 2\mathbf{u}_d^n + \frac{1}{2}\mathbf{u}_d^{n-1}}{\Delta t} = (-\nabla p + \nu\nabla^2\mathbf{u})^{n+1}, \tag{24}$$

where $\mathbf{u}_d^n$ is the velocity $\mathbf{u}$ at the departure point $\mathbf{x}_d^n$ at time level t^n and $\mathbf{u}_d^{n-1}$ is the velocity at the departure point $\mathbf{x}_d^{n-1}$ at time level t^{n-1}. The departure point $\mathbf{x}_d^n$ is obtained by solving (20) with (21) over one single time level Δt; while point $\mathbf{x}_d^{n-1}$ is obtained by solving

$$\frac{d\mathbf{x}}{dt} = \mathbf{u}^n(\mathbf{x}, t), \quad \mathbf{x}(t^{n+1}) = \mathbf{x}_a \tag{25}$$

over two time levels $2\Delta t$. By using the above characteristic equations, the resulting scheme (24) is second-order accurate in time and can be verified by Taylor expansion analysis.

A three-step splitting scheme can be used to solve (24), i.e.,

$$\frac{\hat{\mathbf{u}} - 2\mathbf{u}_d^n + \frac{1}{2}\mathbf{u}_d^{n-1}}{\Delta t} = 0, \tag{26}$$

$$\frac{\hat{\hat{\mathbf{u}}} - \hat{\mathbf{u}}}{\Delta t} = -\nabla p^{n+1}, \tag{27}$$

$$\frac{\frac{3}{2}\mathbf{u}^{n+1} - \hat{\hat{\mathbf{u}}}}{\Delta t} = \nu\nabla^2\mathbf{u}^{n+1}. \tag{28}$$

The discrete divergence-free condition $\nabla \cdot \mathbf{u}^{n+1} = 0$ results in a consistent Poisson equation for the pressure

$$\nabla^2 p^{n+1} = \frac{1}{\Delta t}\nabla \cdot \hat{\mathbf{u}},$$

with accurate pressure boundary conditions of the form [16]

$$\frac{\partial p}{\partial n} = -\nu \cdot \mathbf{n}[\hat{\mathbf{u}} + \nabla \times \omega^{n+1}],$$

where $\mathbf{n}$ is the unit normal, and ω is the vorticity. For details of the solution procedure of the equations, see chapter 8 of [18].

3.3. Numerical Results

In this section, we present numerical results by applying the above discretizations to different benchmark problems. In all the tests employing the SLSE method, the second-order Runge–Kutta method is employed for backward integration.

3.3.1. *The Taylor Vortex*

We use the Taylor vortex problem, an exact solution to the unsteady Navier–Stokes equations, in order to quantify the error in the SLSE method. It has the form

$$u = -\cos x \ \sin y \ e^{-2t/Re}, \tag{29}$$

$$v = \sin x \ \cos y \ e^{-2t/Re}, \tag{30}$$

$$p = -\frac{1}{4}(\cos 2x + \cos 2y)e^{-4t/Re}. \tag{31}$$

The computational domain is a square defined by the coordinates $[-\frac{\pi}{2}, \frac{\pi}{2}]$ in each direction. A mesh consisting of 2×2 quadrilateral elements is used, and the spectral order ranges as $P = 8, 10, 12$, and 14. The Reynolds number is fixed at 10^6, and the L^∞ norm is used to examine the error. Note that despite the high Reynolds number here, this is a relatively simple flow to resolve spatially and also it decays exponentially in time.

In Fig. 9 we show the evolution of the L^∞ error of the solution over long-time integration, starting from exact initial conditions. The Crank–Nicolson SLSE method develops a long-term instability and it leads to inaccurate results. It is seemingly stable for this application because of the decaying of the exact solution with time; in the next section this long-term instability will be documented more clearly. On the other hand, the stiffly-stable SLSE method is robust with accuracy comparable to the Eulerian scheme.

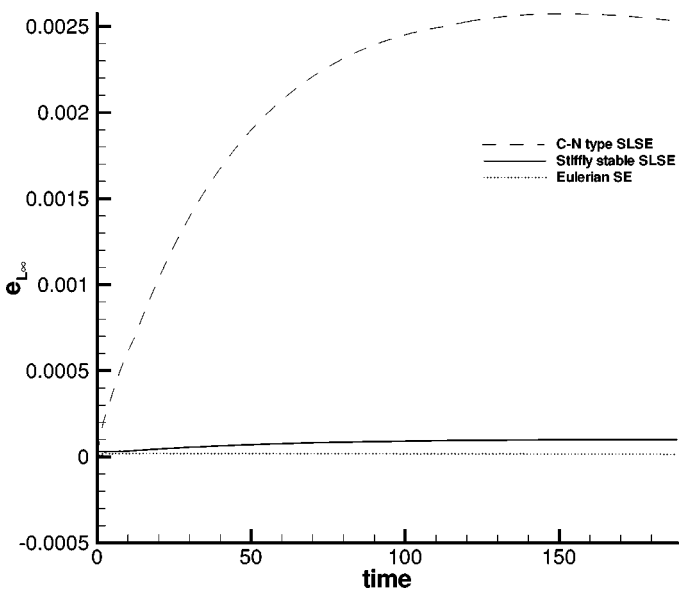

FIG. 9. Time history of error over long-term integration.

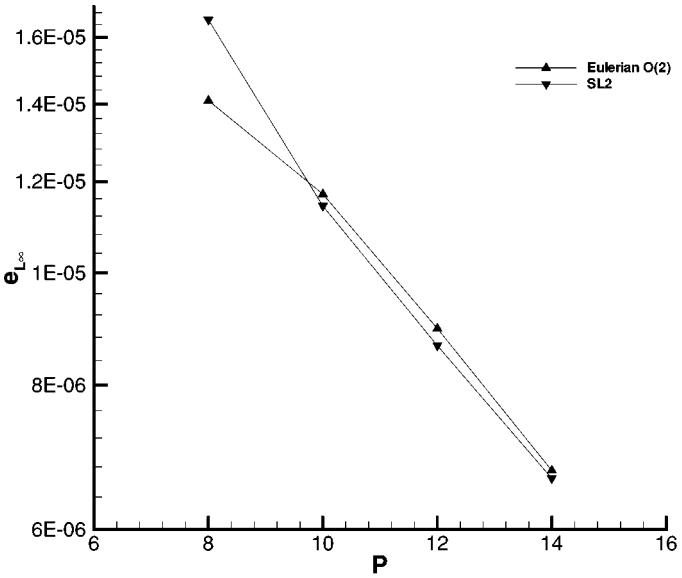

FIG. 10. Spectral convergence for Eulerian SE and SLSE methods.

In Fig. 10 we plot the dependence of the error upon the spectral polynomial order. The L^∞ error of the velocity is measured at $t = 2\pi$, i.e., after one revolution of the flow. We see in this semi-log plot that spectral convergence is achieved by both Eulerian and semi-Lagrangian spectral/*hp* element methods. The time step here is chosen by fixing the CFL number at $\sigma = 0.6$. In Fig. 11 we plot the dependence of the error upon the size of time step for the stiffly-stable method. The results are similar to the behavior reported earlier for the advection–diffusion equation. Note here the accuracy of SLSE method is dictated by the term $\mathcal{O}(\Delta t^2 + \frac{\Delta x^{P+1}}{\Delta t})$. At low P the interpolation error dominates, and increasing Δt decreases the overall error, as shown for $P = 6$. When the interpolation error is small at $P = 12$, the Δt^2 term dominates and further increase in Δt increases the overall error. The $P = 8$ curve shows the competition between these two terms. In this plot, the largest time step 0.03 corresponds to the CFL number about 4. We emphasize that it is the size

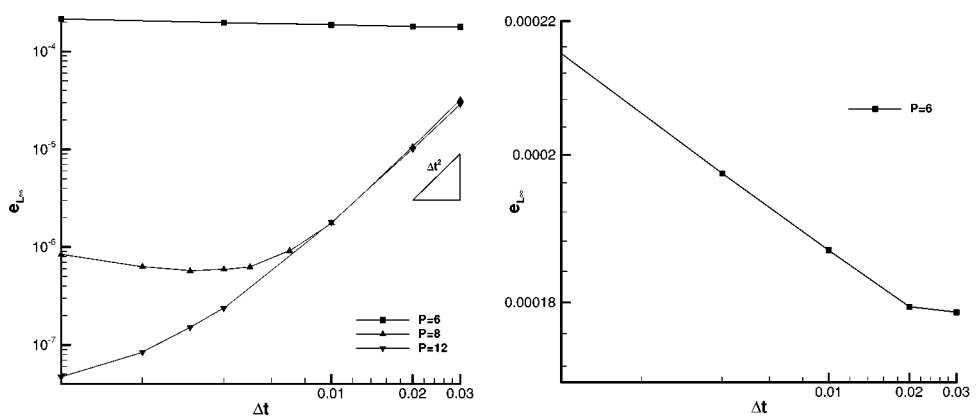

FIG. 11. Error dependence on Δt. Left: SLSE results. Right: close-up view for $P = 6$.

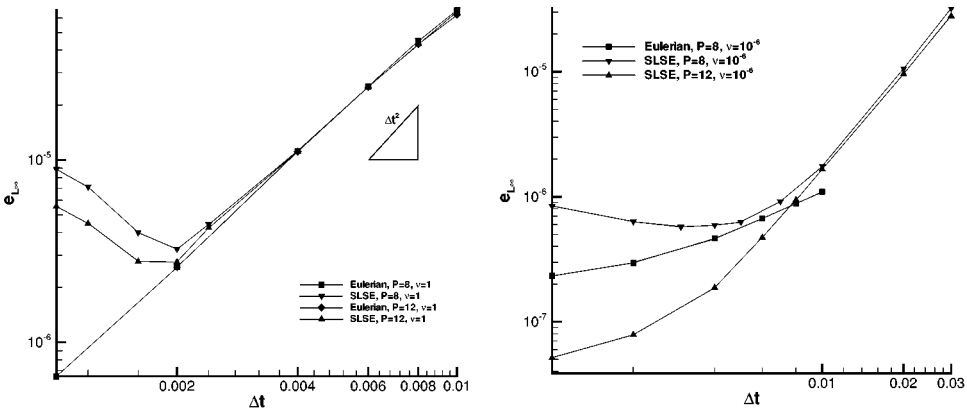

FIG. 12. Error dependence on Δt. Left: $Re = 1$, and Right: $Re = 10^6$.

of Δt and *not* the CFL number that restricts the use of semi-Lagrangian method. In other words, for the SLSE method, the restriction on the size of time step is solely due to accuracy considerations but not due to stability.

In the Navier–Stokes implementation, another contribution to the error that needs to be examined is associated with the splitting procedure (Eq. (26)). For the second-order SLSE method proposed here, the splitting error scales as $\mathcal{O}(\nu \Delta t^2)$. This error is only visible for relatively viscous flows. We use two extreme cases to examine this error: One is at $\nu = 1$ ($Re = 1$) where the splitting error is of the same order as temporal error; the other is at $\nu = 10^{-6}$ ($Re = 10^6$) where the splitting error is negligible. In Fig. 12 we show the results for these two cases, and comparison with the second-order Eulerian method for exactly the same spatial discretization. We see that at $Re = 1$, the $\mathcal{O}(\Delta t^2)$ error dominates at very small time step ($\Delta t \sim 10^{-3}$). However, at $Re = 10^6$ the $\mathcal{O}(\Delta t^2)$ error starts to dominate only at $\Delta t \sim 10^{-2}$. Comparison of the two responses suggests that the $\mathcal{O}(\Delta t^2)$ error observed at $Re = 1$ is the splitting error, and it is comparable in that case to the Runge–Kutta second-order error. The second-order Eulerian method generates the exact same error in this low Re number case and reinforces the above statement. It should be noted that the error from the semi-Lagrangian part, i.e., $\mathcal{O}(\Delta t^2 + \frac{\Delta x^{P+1}}{\Delta t})$, contains another $\mathcal{O}(\Delta t^2)$ term. In advection-dominated flows the Reyolds number is greater than one, and thus the splitting error is always subdominant.

3.3.2. *Two-Dimensional Driven Cavity Flow*

We consider the standard benchmark problem of two-dimensional driven cavity flow; see Fig. 13. The flow is sustained by the motion of the upper wall at constant velocity while all other walls are stationary. A mesh consisting of 10×10 quadrilateral elements is used for most of the tests, and the spectral order is set to $P = 10$. We compare the horizontal velocity profile along the vertical center line and the vertical velocity profile along the horizontal center line in Figs. 14 and 15 corresponding to Reynolds number $Re = 400$ in the first and to $Re = 3{,}200$ and $Re = 10{,}000$ in the second figure. The Reynolds number here is based on the velocity of the upper wall and the height of the cavity. The time step of Eulerian spectral/hp element method is chosen by fixing CFL number at $\sigma = 0.6$, while for SLSE the time step is more than 30 times larger with CFL number at 20. We observe that the

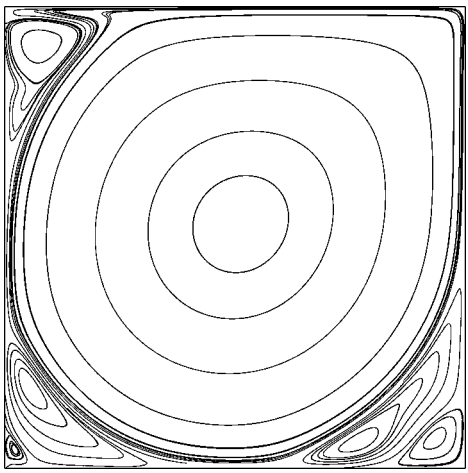

FIG. 13. 2-D driven cavity flow at $Re = 10{,}000$. The flow is (slightly) unsteady so streamlines of the time-averaged flow are shown.

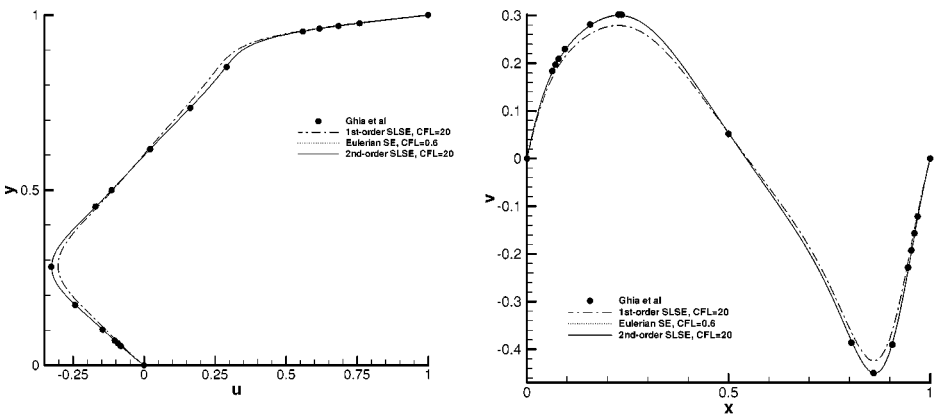

FIG. 14. 2-D driven cavity flow at $Re = 400$. Left: u-velocity profile along vertical centerline. Right: v-velocity profile along horizontal centerline. (Second-order SLSE result in indistinguishable from Eulerian result.)

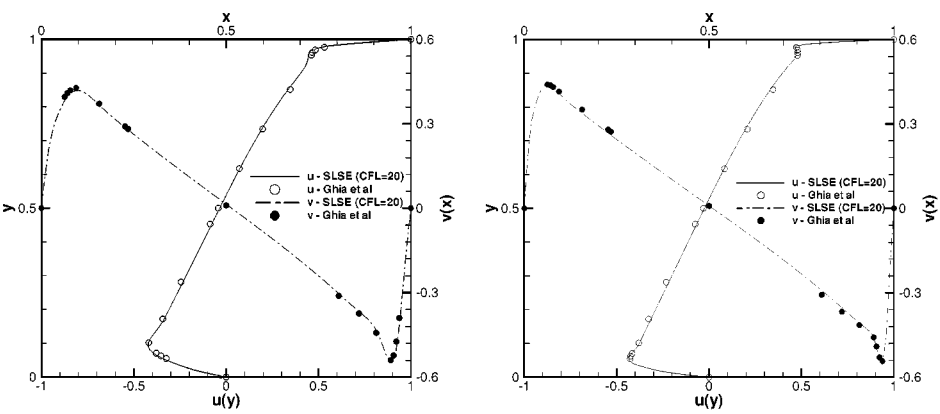

FIG. 15. 2-D driven cavity flow at $Re = 3{,}200$ (left) and $Re = 10{,}000$ (right). Comparisons of the two velocity components along the vertical and horizontal centerline.

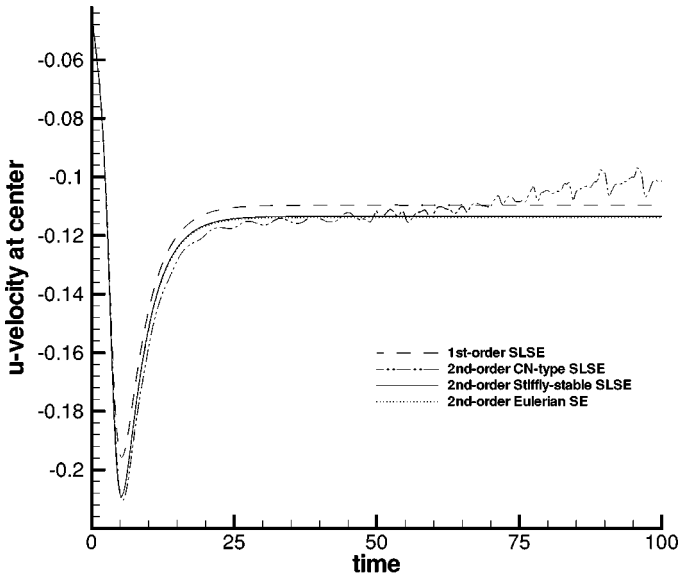

FIG. 16. Time history of u-velocity at the center of the cavity with various methods; $Re = 400$.

semi-Lagrangian and Eulerian methods give essentially identical results, which they agree with the accepted results of [12]. At $Re = 400$ we included results from a first-order SLSE that show visible differences with the high-order accurate results. At $Re = 10{,}000$ the flow has bifurcated to an unsteady state. A time periodic oscillation is established, consistent with the results of bifurcation studies for the driven cavity flow (see, for example, [33]). In Fig. 15 (right) the velocity profiles at $Re = 10{,}000$ correspond to the time-averaged values; they agree with the steady state solution of [12] as the onset of bifurcation is just below $Re = 10{,}000$.

We now return to $Re = 400$ to investigate the stability of the Crank–Nicolson semi-Lagrangian scheme. In Fig. 16 we plot the time history of the horizontal-velocity at the center point of the cavity after *long-time integration*. The flow reaches steady state after $t \sim 30$ (nondimensional convective time units). We can see that the second-order stiffly-stable SLSE method gives almost identical results as the second-order Eulerian method. The first-order SLSE method also reaches steady state but gives less accurate results. However, the second-order Crank–Nicolson SLSE method develops a weak long-term instability and fails to reach a steady state in the end, although at an earlier time ($t \sim 50$) it actually approximates the solution better than the stable first-order method.

We finally compare results for the semi-Lagrangian method using linear and quadratic triangular finite elements for first- and second-order (in time). The results shown in Fig. 17 were obtained on a mesh consisting of 32×64 equal triangular elements. We see that even in the limit of low polynomial order the second-order semi-Lagrangian method performs quite accurately in contrast with the first-order (in time) semi-Lagrangian method.

3.3.3. *Three-Dimensional Driven Cavity Flow*

The extension of the SLSE method to three dimensions is straightforward. Here we study the effect of the three-dimensionality in the driven cavity flow as a function of the aspect

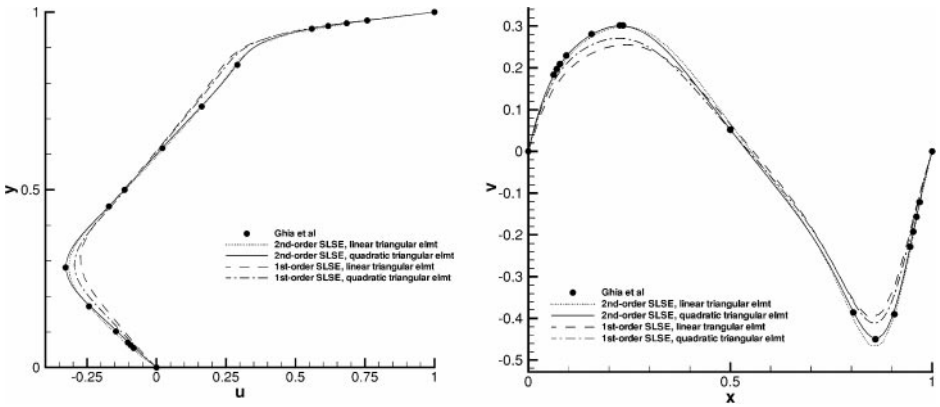

FIG. 17. 2-D driven cavity flow at $Re = 400$ for linear and quadratic (triangular) elements. Left: u-velocity profile along vertical centerline. Right: v-velocity profile along horizontal centerline.

ratio. The Reynolds number is set at 400 and the aspect ratio was set to 1, 3, and 5. We plot velocity profiles at the center symmetric plane in Fig. 18. Three-dimensionality effects are more pronounced, as expected, for the expansion ratio 1 as the results deviate the most from the corresponding two-dimensional profile, while for the aspect ratio 5, a trend toward two-dimensionality is observed. The results shown in the figure are obtained by SLSE method with CFL number 20. Results of the Eulerian spectral/hp element method are also computed with CFL number at 0.6 but are not shown in the plot because they are essentially identical as the SLSE results. In [2], the semi-Lagrangian (quadratic) finite element method is used to solve the 2D driven cavity flow. The reported results show significant difference with the results of [12], and the authors claim favorable comparison with three-dimensional experimental results of [19]. The present simulations of the three-dimensional driven cavity flow suggest that such an agreement may have been fortuitous.

3.3.4. *Transitional Flow Past a Square Cylinder*

In this example, we test the method in the context of vortex shedding for flow past a square cylinder, which becomes transitional even at low Reynolds number. Specifically,

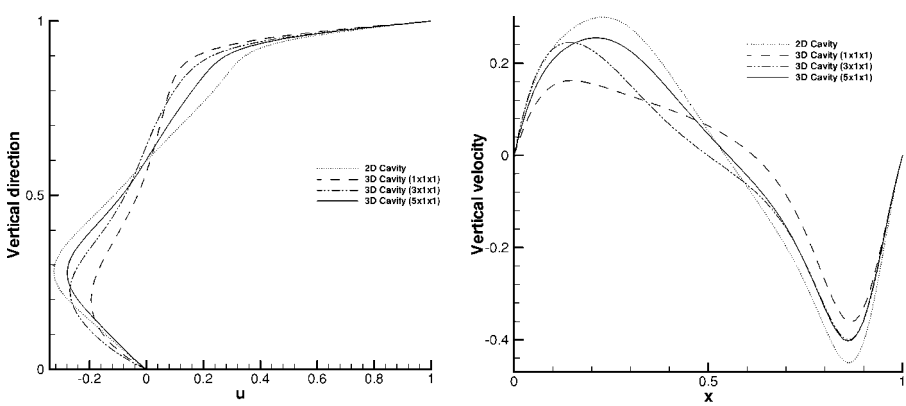

FIG. 18. 3-D driven cavity flow at $Re = 400$. Left: Horizontal-velocity profile along vertical centerline, Right: vertical-velocity profile along horizontal centerline.

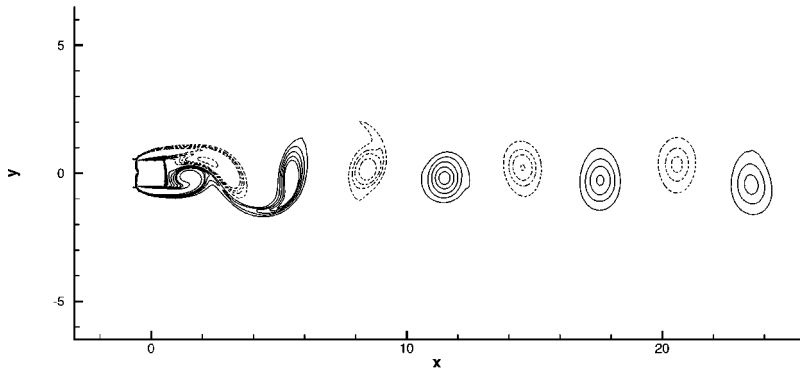

FIG. 19. Snapshot of vorticity contours at $Re = 200$. (Dotted lines denote negative vorticity.) A "2S" vortex shedding mode is observed.

we will compare with results of Eulerian schemes as well as experimental results cited in [8, 10, 26, 32, 35]. The flow remains steady until the Reynolds number reaches its first critical value at around $40 \sim 50$. Here the Reynolds number is based on the uniform inflow and length of the square cylinder. Above $Re \sim 50$ a periodic vortex shedding is observed as shown in Fig. 19. At higher Reynolds number, because of the fast transition that takes place with a subharmonic cascade present, there is disagreement in the published results related to the Strouhal number, and drag and lift coefficients. Here we simulate this flow in the Reynolds number range from 20 to 300 but we only report results for the most interesting cases.

In Fig. 20 we show the element mesh employed in the simulations. It consists of 1502 triangles with the smaller size elements concentrated around the cylinder in order to capture the large gradients of vorticity caused by the sharp corners. This is the highest resolution mesh used in [7] in their three-dimensional simulation of a square-section cylinder with a wavy surface. They employed the same spectral/hp element code as the one here but with

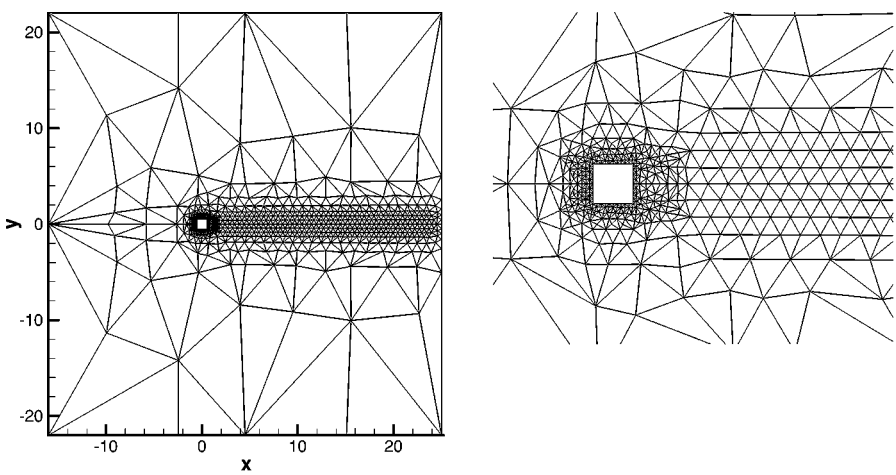

FIG. 20. Element mesh for flow past a square cylinder. Left: Entire domain (1502 triangles). Right: Close-up view near the cylinder.

TABLE II
Comparison of Strouhal Number (*B* is the Blockage Ratio)

Re	SLSE $B = 2.3\%$	Eulerian SE $B = 2.3\%$	Okajima [26] (experimental) $B = 0\%$	Saha [32] (numerical) $B = 10\%$	Davis [8] (numerical) $B = 0\%$	Franke [10] (numerical) $B = 8.3\%$	Sohankar [36] (numerical) $B = 5.6\%$
100	0.146	0.145	0.141–0.145	0.159	0.154	—	—
200	0.148	0.147	0.138–0.145	0.163	—	0.157	0.170
250	0.139	0.138	0.139–0.143	0.142	0.165	0.141	0.154
300	0.136	0.136	0.137–0.139	0.146	—	0.130	0.138

the Eulerian version, and they simulated flows up to $Re = 150$. The domain size parameters $L_i = 16$ (inflow), $L_o = 25$ (outflow), and $L_h = 22$ (crossflow) result in a low blockage ratio ($B = 1/2L_h = 2.3\%$), and are chosen according to the study in [3]. All lengths are nondimensionalized here with respect to the size of the cylinder. We carried out a detailed convergence study, similar to the one in [7], confirming that with polynomial order $P \geq 6$ a resolution-independent solution is obtained.

The time step for SLSE is $0.005 \sim 0.01$, depending upon the exact value of the Reynolds number and the polynomial order, and is at least ten times larger than the corresponding Eulerian SE runs. Increasing the Reynolds number leads to increases of velocity amplitudes, and this explains such dependence. The restriction on the time step for SLSE is a concern of accuracy but not stability. In Table II we compare the Strouhal number (nondimensional frequency) of vortex shedding at different Reynolds numbers. It can be seen that SLSE gives results very close to the Eulerian SE method, and they both agree with Okajima's experimental result well [26]. The discrepancy with other computational results reported in the literature is due to their larger blockage ratio, i.e., smaller size of the domain, and also lower spatial resolution. It should be noted that most of earlier computations are performed with low-order methods.

At $Re = 100$ and 200, the flow is periodic with a single vortex shedding frequency, but with the higher *Re* flow exhibiting stronger super-harmonics. However, at $Re = 300$ the flow loses stability and a subharmonic frequency cascade emerges. Figure 21 shows

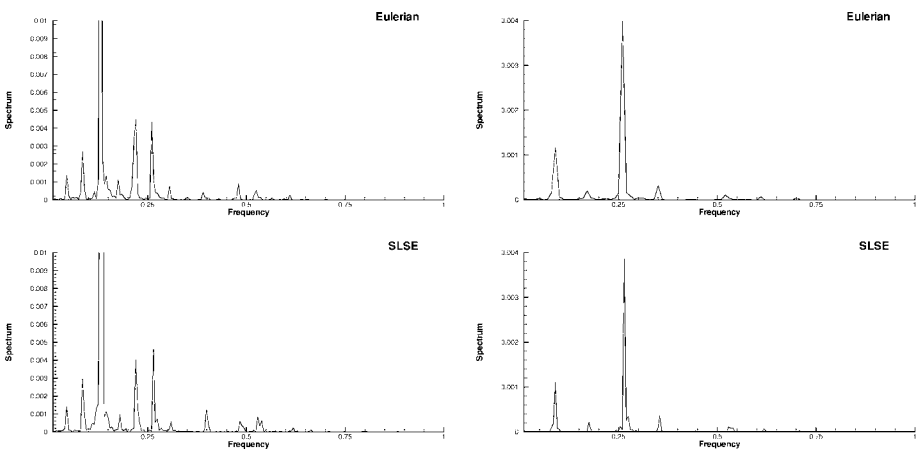

FIG. 21. Spectra of transverse velocity and pressure in the near-wake at $Re = 300$ from SLSE and Eulerian SE method. Left: Transverse velocity spectrum. Right: Pressure spectrum.

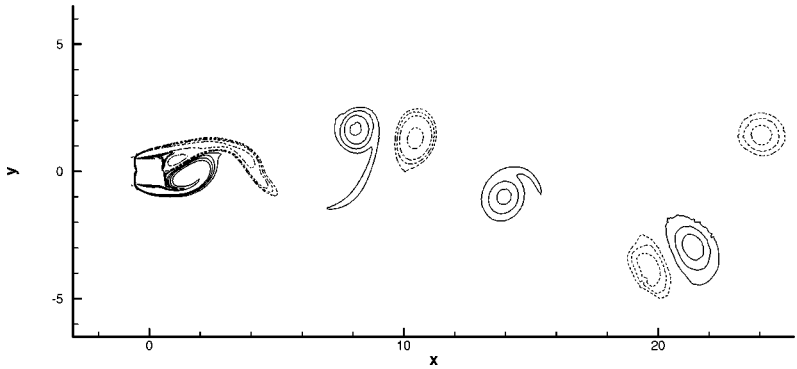

FIG. 22. Snapshot of vorticity contours at $Re = 300$. (Dotted lines denote negative vorticity). A "$(2P + 2S)$" vortex shedding mode is observed.

the amplitude spectra of transverse velocity and corresponding pressure at $Re = 300$. The time-history is gathered at a near-wake point ($x = 3.43$, $y = 0.83$). The results from the semi-Lagrangian method and Eulerian method agree very well. They both show clearly the presence of subharmonics with the existence of lower frequency of $1/3$ of the primary shedding frequency. For the transverse velocity spectra on the left, the primary shedding frequency is $f_b = 0.136$ and the two subharmonics are $f_1 \approx 0.045$ and $f_2 \approx 0.09$.

Figure 22 shows a snapshot of vorticity contours at $Re = 300$. The flow pattern is in accordance with the "(2P + 2S)" vortex shedding mode discovered in experiments in [39] for an oscillating circular cylinder. In this pattern, two vortices of opposite vorticity form a pair on either side of the centerline while a single vortex is formed between the pair. The corresponding subharmonics in the experiments were also one-third of the primary frequency. Williamson and Roshko have presented the physical reasons for this spatio-temporal behavior [39]. Note that the normal mode of shedding is similar to what is shown in Fig. 19, which is termed as the "2S" mode. In this pattern, a single vortex of opposite vorticity is formed on either side of the centerline.

As regards computational efficiency, a *twenty times* larger time step was employed in the SLSE simulation compared to the Eulerian simulation with other identical parameters. The corresponding computational speed up with the SLSE method was a factor of about four, without any special code optimization.

4. SUMMARY

A semi-Lagrangian spectral/*hp* element (SLSE) method was presented and applied to advection–diffusion and incompressible Navier–Stokes equations. The method is free from the CFL-restriction and thus very large time steps can be used, dictated only by accuracy considerations. This should not be interpreted as violation of the CFL condition, as the numerical domain of dependence of the solution still contains its domain of dependence [9]. It can be understood by considering the definition of the CFL condition on a *fixed* number of nodes as in the finite difference approximations, and contrasting it with the effectively *variable* stencil involved in the semi-Lagrangian approach.

An interesting aspect of the method is the structure of the temporal (advection) error, which reveals nonmonotonic trend with the time step. In particular, in a certain range of

parameters typically encountered in practical computations, the overall error decreases as the time step increases. This behavior, however, depends on the interpolation procedure involved and inaccurate representations may mask this trend. From the practical point of view, it is the capability of employing significantly larger time steps compared with the Eulerian schemes that make the SLSE method particularly attractive, especially for high Reynolds number simulations. This comes at the expense of extra interpolations, which are "intrinsic" in the spectral/*hp* element method, but it avoids prohibitive costs associated with nonsymmetric solvers as in fully implicit schemes or remeshing as in purely Lagrangian approaches. The high-order spatial discretization of the spectral/*hp* element method seems to significantly enhance the possibility of using very large time steps. In our numerical tests, the CFL number can be as high as $20 \sim 30$ and still retain good accuracy, while the semi-Lagrangian method with finite elements is about $6 \sim 7$ [37]. The total cost of SLSE method was found to be an order of magnitude less than the Eulerian method, depending on the specific problem. This result is more favorable than the cost reported in [4], where relatively low-order spatial discretizations and explicitly constructed interpolation algorithms were employed.

The SLSE method was also extended to incompressible Navier–Stokes equations with focus on second-order temporal accuracy. Two different types of second-order SLSE methods were presented, and it was shown that only the stiffly-stable implementation is suitable for practical applications. Numerical results with the Taylor vortex problem and two- and three-dimensional cavity flows demonstrated a similar error structure as in the advection–diffusion equation. A transition flow past a square cylinder in a regime where strong subharmonics are present was also simulated. A time step of twenty times larger was used and an overall speed up factor of *four* was obtained compared to corresponding Eulerian time-stepping. The advantages of semi-Lagrangian methods, however, should be demonstrated in direct numerical simulation of *inhomogeneous* turbulent flows, where the time step currently used is two to three orders of magnitude smaller than the Kolmogorov temporal scale. While the overall gain for homogeneous flows employing Fourier discretizations may be marginal, consistent with the estimates of Eq. (1) and the analysis in [4], we expect a large gain for complex-geometry turbulent flows requiring nonuniform grids. We will report on such systematic studies in a future publication.

ACKNOWLEDGMENTS

The authors thank R. M. Kirby, F. Bisshop, and F. X. Giraldo for their useful suggestions. We also want to thank the anonymous referees for their valuable suggestions including several references from the meteorological literature. This work was supported partially by ONR, DOE, and NSF. The computations were performed on the SGI O2000 at NCSA, University of Illinois at Urbana-Champaign, and at Brown's Center for Scientific Computing & Visualization.

REFERENCES

1. Y. Achdou and J. L. Guermond, Convergence analysis of a finite element projection/Lagrange–Galerkin method for the incompressible Navier–Stokes equations, *SIAM J. Numer. Anal.* **37**, 799 (2000).
2. A. Allievi and R. Bermejo, Finite element modified method of characteristics for the Navier–Stokes equations, *Int. J. Numer. Methods Fluids* **32**, 439 (2000).
3. D. Barkley and R. D. Henderson, Three-dimensional Floquet stability analysis of the wake of a circular cylinder, *J. Fluid Mech.* **322**, 215 (1996).

4. P. Bartello and S. J. Thomas, The cost-effectiveness of semi-Lagrangian advection, *Mon. Wea. Rev.* **124**, 2883 (1996).
5. G. Brassington and B. Sanderson, Semi-Lagrangian and COSMIC advection in flows with rotation or deformation, *Atmos.-Ocean.* **37**, 369 (1999).
6. D. Chu and G. E. Karniadakis, A direct numerical simulation of laminar and turbulent flow over riblet-mounted surfaces, *J. Fluid Mech.* **250**, 1 (1993).
7. R. M. Darekar and S. J. Sherwin, Flow past a square section cylinder with a wavy stagnation face, *J. Fluid Mech.* **426**, 263 (2001).
8. R. W. Davis, E. F. Moore, and L. P. Purtell, A numerical-experimental study of confined flow around rectangular cylinders, *Phys. Fluids* **27**, 46 (1984).
9. M. Falcone and R. Ferretti, Convergence analysis for a class of high-order semi-Lagrangian advection schemes, *SIAM J. Numer. Anal.* **35**, 909 (1998).
10. R. Franke, W. Rodi, and B. Schönung, Numerical calculation of laminar vortex-shedding flow past cylinders, *J. Wind Eng. Indust. Aero.* **35**, 237 (1990).
11. G. W. Gear, *Numerical Initial Value Problems in Ordinary Differential Equations* (Prentice Hall, New York, 1971).
12. U. Ghia, K. N. Ghia, and C. T. Shin, High-*Re* solutions for the incompressible flow using the Navier–Stokes equations and a multigrid method, *J. Comput. Phys.* **48**, 387 (1982).
13. F. X. Giraldo, The Lagrange-Galerkin spectral element method on unstructured quadrilateral grids, *J. Comput. Phys.* **147**, 114 (1998).
14. L. C. Huang, Problem of the pressure correction projection method—additional notes to our 6ISCFD paper, in Institute of Computational Mathematics and Scientific/Engineering Computing (Chinese Academy of Sciences, 1995).
15. J. P. Huffenus and D. Khaletzky, A finite element method to solve the Navier–Stokes equations using the method of characteristics, *Int. J. Numer. Methods Fluids* **4**, 247 (1984).
16. G. E. Karniadakis, M. Israeli, and S. A. Orszag, High-order splitting methods for the incompressible Navier–Stokes equations, *J. Comput. Phys.* **97**, 414 (1991).
17. G. E. Karniadakis and S. A. Orszag, Nodes, modes, and flow codes, *Physics Today* **March**, 34 (1993).
18. G. E. Karniadakis and S. J. Sherwin, *Spectral/hp Element Methods for CFD* (Oxford Univ. Press, London, 1999).
19. J. R. Koseff and R. L. Street, The lid-driven cavity flow: a synthesis of qualitative and quantitative observations, *ASME J. Fluids Eng.* **106**, 390 (1984).
20. A. V. Malevsky, Spline-characteristic method for simulation of convective turbulence, *J. Comput. Phys.* **123**, 466 (1996).
21. A. V. Malevsky and S. J. Thomas, Parallel algorithms for semi-Lagrangian advection, *Int. J. Numer. Meth. Fluids* **25**, 455 (1997).
22. Ma Xia, G. S. Karamanos, and G. E. Karniadakis, Dynamics and low-dimensionality of turbulent near-wake, *J. Fluid Mech.* **410**, 29 (2000).
23. A. McDonald, Accuracy of multi-upstream, semi-Lagrangian advective schemes, *Mon. Wea. Rev.* **112**, 1267 (1984).
24. A. McDonald and J. R. Bates, Improving the estimate of the departure point position in a two-time level semi-Lagrangian and semi-Implicit scheme, *Mon. Wea. Rev.* **115**, 737 (1987).
25. J. L. McGregor, Economical determination of departure points for semi-Lagrangian models, *Mon. Wea. Rev.* **121**, 221 (1993).
26. A. Okajima, Strouhal numbers of rectangular cylinders, *J. Fluid Mech.* **123**, 379 (1982).
27. A. Oliveira and A. M. Baptista, A comparison of integration and interpolation Eulerian-Lagrangian methods, *Int. J. Numer. Methods Fluids* **21**, 183 (1995).
28. O. Pironneau, On the transport-diffusion algorithm and its applications to the Navier–Stokes equations, *Numer. Math.* **38**, 309 (1982).
29. A. Priestley, Exact projections and the Lagrange-Galerkin method: A realistic alternative to Quadrature, *J. Comput. Phys.* **112**, 316 (1994).

30. J. Pudykiewicz, R. Benoit, and A. Staniforth, Preliminary results from a partial LRTAP model based on an existing meteorological forecast model, *Atmos.-Ocean* **23**, 267 (1985).
31. A. Robert, A stable numerical integration scheme for the primitive meteorological equations, *Atmos.-Ocean.* **19**, 35 (1981).
32. A. K. Saha, K. Muralidhar, and G. Biswas, Transition and chaos in two-dimensional flow past a square cylinder, *J. Eng. Mech.* **126**, 523 (2000).
33. J. Shen, Hopf bifurcation of the unsteady regularized driven cavity flow, *J. Comput. Phys.* **95**, 228 (1991).
34. P. K. Smolarkiewicz and J. Pudykiewicz, A class of semi-Lagrangian approximations for fluids, *J. Atms. Sci.* **49**, 2082 (1992).
35. A. Sohankar, C. Norberg, and L. Davidson, Low-Reynolds-number flow around a square cylinder at incidence: study of blockage, onset of vortex shedding and outlet boundary condition, *Int. J. Numer. Methods Fluids* **26**, 39 (1998).
36. A. Sohankar, C. Norberg, and L. Davidson, Simulation of three-dimensional flow around a square cylinder at moderate Reynolds numbers, *Phys. Fluids* **11**, 288 (1999).
37. A. Staniforth and J. Côté, Semi-Lagrangian integration schemes for atmospheric models-A review, *Mon. Wea. Rev.* **119**, 2206 (1991).
38. E. Süli, Convergence and nonlinear stability of the Lagrange-Galerkin method for the Navier–Stokes equations, *Numer. Math.* **53**, 459 (1988).
39. C. H. K. Williamson and A. Roshko, Vortex formation in the wake of an oscillating cylinder, *J. Fluid Struct.* **2**, 355 (1988).